JACS
JOURNAL OF THE AMERICAN CHEMICAL SOCIETY
pubs.acs.org/JACS
Article

Surface Lattice Modulation through Chemical Delithiation toward a Stable Nickel-Rich Layered Oxide Cathode

Si-Qi Lu, Qinghua Zhang, Fanqi Meng, Ya-Ning Liu, Jianjun Mao, Sijie Guo, Mu-Yao Qi, Yan-Song Xu, Yan Qiao, Si-Dong Zhang, Kecheng Jiang, Lin Gu, Yang Xia, Shuguang Chen, GuanHua Chen, An-Min Cao,* and Li-Jun Wan*

Cite This: J. Am. Chem. Soc. 2023, 145, 7397−7407

Read Online

ACCESS | Metrics & More | Article Recommendations | Supporting Information

ABSTRACT: Nickel-rich layered oxides (NLOs) are considered as one of the most promising cathode materials for next-generation high-energy lithium-ion batteries (LIBs), yet their practical applications are currently challenged by the unsatisfactory cyclability and reliability owing to their inherent interfacial and structural instability. Herein, we demonstrate an approach to reverse the unstable nature of NLOs through surface solid reaction, by which the reconstructed surface lattice turns stable and robust against both side reactions and chemophysical breakdown, resulting in improved cycling performance. Specifically, conformal $La(OH)_3$ nanoshells are built with their thicknesses controlled at nanometer accuracy, which act as a Li^+ capturer and induce controlled reaction with the NLO surface lattices, thereby transforming the particle crust into an epitaxial layer with localized Ni/Li disordering, where lithium deficiency and nickel stabilization are both achieved by transforming oxidative Ni^{3+} into stable Ni^{2+}. An optimized balance between surface stabilization and charge transfer is demonstrated by a representative NLO material, namely, $LiNi_{0.83}Co_{0.07}Mn_{0.1}O_2$, whose surface engineering leads to a highly improved capacity retention and excellent rate capability with a strong capability to inhibit the crack of NLO particles. Our study highlights the importance of surface chemistry in determining chemical and structural behaviors and paves a research avenue in controlling the surface lattice for the stabilization of NLOs toward reliable high-energy LIBs.

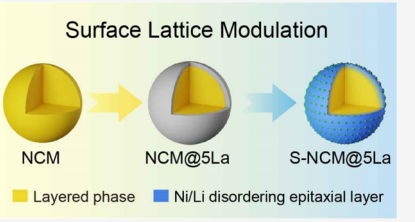

INTRODUCTION

High-performance lithium-ion batteries (LIBs) have found enormous applications in portable devices, electric vehicles, and smart grids.[1−4] Along with the pursuit of high energy density, Ni-rich layered oxides (NLOs) are widely acknowledged as a type of promising cathode materials owing to their dual advantages by providing high reversible capacity while curtailing the content of high-cost cobalt.[5−8] Despite their great industrial interest, the NLO electrodes suffer from continuous capacity fading during extended electrochemical cycles, which leads to inherent stability and reliability challenges when coupled with serious chemophysical breakdown of the NLO particles.[9−11] Typically, Ni^{4+} species generated from the charging process are highly reactive and are susceptible to parasitic reactions with organic electrolytes, inducing a continuous dissolution of transition metals (TMs) and a gradual consumption of electrolytes.[12,13] As a result, thick cathode−electrolyte interphase (CEI) layers are consequently formed around the NLO particles to hinder the transfer of Li^+, leading to further interfacial polarization and cycling capability deterioration.[13,14] Meanwhile, the NLO particles usually undergo a structural phase transformation from the H2 phase to the H3 phase when charged with a high voltage of up to 4.2−4.3 V.[15−17] The associated structural degradation together with the large anisotropic volume change exerts mechanical strain on the NLO particles during the continuous charge/discharge process, which thereby become prone to cracks and expose fresh surfaces for further side reactions.[18,19] The close interweaving of a large variety of degradation factors renders the NLOs inherently unstable, whose structural failures are considered to mainly stem from the complicated cathode−electrolyte interface, followed by a gradual inward propagation to the final exhaustion of all the active particles.[20,21]

In view of the critical role played by the surface chemistry of NLO particles, suitable surface treatment becomes indispensable to combat interfacial and structural degradation before their electrochemical applications.[22] Accordingly, surface coating is a straightforward protocol that has been generally resorted to for NLO stabilization.[23,24] Despite the intense recent efforts on surface engineering of NLOs, a clear picture of the surface physicochemical properties and their corresponding functions remains very scarce due to the complicated nature of the surface, which is meanwhile vulnerable to environmental conditions.[25−27] On the one hand, the NLO

Received: December 27, 2022
Published: March 24, 2023

https://doi.org/10.1021/jacs.2c13787
J. Am. Chem. Soc. 2023, 145, 7397−7407

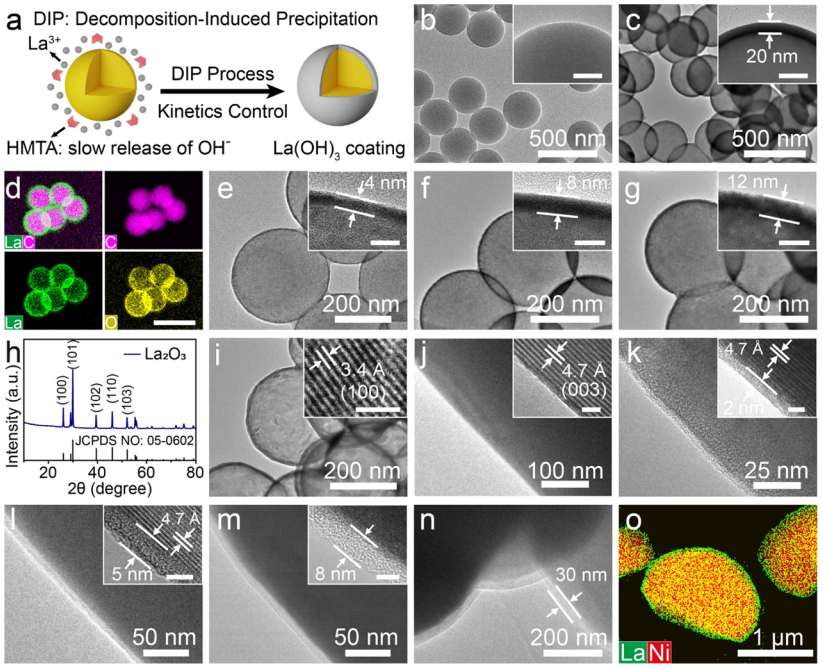

Figure 1. Fabrication processes and characterization of $La(OH)_3$ nanoshells. (a) Schematic illustration of the DIP process to build $La(OH)_3$ nanoshells. The slow decomposition of HMTA released the hydroxyl group for the precipitation of La in a controlling way, forming a uniform $La(OH)_3$ coating with good control on the growth kinetics. TEM image of polystyrene nanospheres as the seeds before (b) and after (c) the coating process. The insets are the corresponding highly magnified TEM images for surface details. The scale bars in the inset of (b,c) both indicate 50 nm. (d) Elemental mappings analysis of surface-coated PS nanospheres to reveal the formation of a uniform $La(OH)_3$ nanoshell. The scale bar indicates 500 nm. TEM images of different PS@$La(OH)_3$ samples whose shells are precisely controlled at different levels: 4 (e), 8 (f), and 12 nm (g). The insets show the corresponding high-resolution TEM (HRTEM) images. The scale bars in the inset of (e−g) indicate 5 nm. XRD (h) and TEM (i) results of the produced hollow La_2O_3 nanospheres after the PS removal. The HRTEM image (inset in i) shows a lattice spacing of 3.4 Å for the (100) planes of La_2O_3. The scale bar in the inset of (i) indicates 2 nm. (j) TEM image of a randomly picked particle for the NCM0.83 sample. The particle surface is clean without coating as revealed by the HRTEM analysis (inset in j), which shows a lattice spacing of 4.7 Å for the layered (003) planes. (k−n) TEM images of $La(OH)_3$-coated NCM0.83 with different shell thicknesses: 2 (k), 5 (l), 8 (m), and 30 nm (n). Insets are the corresponding HRTEM images. The scale bars in the inset of (j−m) indicate 2, 2, 5, and 5 nm, respectively. (o) Elemental mappings for La and Ni of the randomly selected NCM@5La samples.

powder has undesirable high sensitivity to both air and moisture.[28] This setback makes the surface treatment of NLO materials a challenging process due to the facile irreversible structural damage, which is particularly troublesome as most water-based procedures become inappropriate.[29] On the other hand, the NLO surface properties are complex, especially considering their high thermal and chemical instability, which makes it difficult to achieve a precise control of the surface structure with clear morphological characters and mediate the structure-performance analysis.[30] To cope with these issues, vacuum-based techniques such as atomic layer deposition (ALD) reasonably emerge as powerful tools widely adopted to treat NLO powder.[31] Consequently, it becomes feasible to ensure a uniform coating of functional materials with high precision while avoiding the risk of ambient exposure. For example, Xu et al. have recently introduced a poly(3,4-ethylenedioxythiophene) (PEDOT) coating onto the surface of a typical Ni-rich cathode, namely, $LiNi_{0.85}Co_{0.1}Mn_{0.05}O_2$ via ALD treatment.[32] By tuning the thickness of the PEDOT nanoshells, the modified sample exhibited a stable cathode−electrolyte interface with much-suppressed side reactions, enabling an improvement of over 30% regarding capacity retention after 100 cycles. It is convincing that a coating treatment can contribute to the interfacial and electrochemical stability. However, the construction of an extra physical barrier between the NLO particles and the electrolyte meanwhile arouses new issues such as interfacial Li^+ transportation and durability of the coating species.[33] In the pursuit of a superior NLO surface, it becomes stringent to explore the possibility of a direct transformation of the surface lattices of NLO into those that are Li^+ conductive and more chemically stable. Such a protocol is promising to build an inherently robust cathode material but currently remains a topic rarely discussed to the best of our knowledge.

Herein, we demonstrated a stable NLO cathode achieved by the surface delithiation strategy, by which the layer-structured lattice was reconstructed into a Ni/Li disordering epitaxial layer (NDEL) with an extraordinary capability to fight against both side reactions and chemophysical degradation. To achieve a clear description of the surface change, we first managed to build a uniform $La(OH)_3$ nanoshell around a representative cathode material formulated as $LiNi_{0.83}Co_{0.07}Mn_{0.1}O_2$ (NCM0.83). The shell thickness was controlled at nanometer accuracy through a wet chemistry route, where an anhydrous solution was used with a delicate growth-kinetics design to ensure a precise coating capability without affecting the moisture-sensitive structure of NCM0.83. A following sintering process initiated the delithiation of NCM0.83 surface at high temperatures, forming a surface-renovated, bulk-unchanged NCM0.83 particles decorated by Li-conductive $LiLaO_2$ nanoparticles. It was found that the surface went through a localized phase transition upon surface reaction. Although a deep delithiation would degrade the surface into an inactive rock-salt phase which was Li-inconductive and lose capacity,

https://doi.org/10.1021/jacs.2c13787
J. Am. Chem. Soc. 2023, 145, 7397−7407

the flexibility in precise nanoshell construction made it possible to take advantage of the benefits from a surface-localized Ni/Li disordering, where lithium deficiency and nickel stabilization were both achieved during the transformation of oxidative Ni^{3+} into stable Ni^{2+}. The experimental and theoretical analyses demonstrated that this reconstructed surface had much lower reactivity with organic electrolytes and was able to ensure a stable cathode−electrolyte interface with lowered polarization and diminished byproducts from parasitic reactions. Notably, such a fortified lattice combined with $LiLaO_2$ on the surface showed the extraordinary capability to not only mitigate the painstaking irreversible phase transformation but also made the NCM0.83 particles mechanically stable to suppress the formation of microcracks, thereby ensuring a much-improved cycling capability (80.8% after 400 cycles at 1 C compared to 35.5% of the control sample) and excellent rate performance (144.2 mAh g^{-1} at 5 C, 116.4 mAh g^{-1} for the control sample). A pouch-type full cell comprising the modified cathode and graphite anode exhibited only 8.7% capacity loss after 100 cycles at 0.5 C in the 3−4.25 V range at 30 °C. This article not only discloses the complexity and importance of surface nature in determining the electrochemical behavior but also inspires new research endeavors to build inherently robust cathode materials for future high-energy applications.

RESULTS AND DISCUSSION

Figure 1a shows a schematic illustration of our synthesis process for the creation of $La(OH)_3$ nanoshells, which follows wet-chemistry protocols in line with our continuous pursuit of alternative techniques for ALD. Considering the fact that the structure of moisture-sensitive NLOs is easily destroyed by an aqueous solution, we switched to anhydrous solvents, particularly ethanol, as the reaction medial so as to eliminate the risk of structural damage during the coating treatment. Briefly, hexamethylenediamine (HMTA) was identified as a decisive agent effective for the controlled precipitation of La^{3+} in the solution. Heating the solution to 60 °C triggered a gradual decomposition of HMTA,[34,35] which released the hydroxyl group to initiate a slow formation of $La(OH)_3$ as the precipitate. It was found that such a decomposition-induced precipitation (DIP) mechanism was highly efficient to control the growth kinetics of $La(OH)_3$, whose growth favorably falls into a heterogeneous pattern, leading to a reliable coating effect on the preexisting seeds in the solution to form the desired core−shell-type produce (Core@$La(OH)_3$). To have a better portrait of the coating capability, we used polystyrene (PS) nanospheres as seeds, whose uniform shape is beneficial to manifest the surface features. Transmission electron microscopy (TEM) analysis displayed that these PS particles were around 350 nm in size (Figure 1b) with a clean and smooth surface (inset in Figure 1b). After a typical coating treatment (see the Supporting Information for experimental details), an outer layer with the thickness around 20 nm appeared around each PS particle (Figure 1c). The high-resolution TEM (HRTEM) analysis (Figure S1) revealed that the coating was amorphous without characteristic lattice fringes, which agrees well with the X-ray diffraction (XRD) characterization of the powder (Figure S2). Further elemental mapping of the coated sample by means of energy dispersive spectroscopy (EDS) confirmed that the outer shell consisted of mainly La and O (Figure 1d), detailing a successful deposition of lanthanum hydroxide around the PS seeds (PS@$La(OH)_3$). Our detailed TEM analysis on a large variety of coated particles found that the coated particles were the only product without the existence of independent particles of $La(OH)_3$.

Such a simple but effective DIP process endows us with a flexible and reliable capability to regulate the morphology of the shells by varying the reaction parameters in the solution. For example, we can adjust the shell thickness on a nanometer scale by just varying the amount of PS seeds while keeping the other reaction conditions unchanged. As shown in Figure 1e, a much thinner nanoshell of 4 nm could be produced when more PS powder was introduced. Similarly, nanoshells of 8 nm and 12 nm, respectively, in thickness were also conveniently prepared by following this regulation approach as demonstrated in Figure 1f,g. After the coating, the PS core could be removed through a heat treatment at 500 °C in an air flow to leave behind the inorganics. As for the PS@20 nm $La(OH)_3$ sample, its sintering formed pure hexagonal phased La_2O_3 (XRD analysis in Figure 1h, PDF no. 05-0602) with a characteristic hollow shape (Figure 1i). Further HRTEM analysis of the wall structure showed obvious lattice fringes with spacing measured to be around 3.4 Å, which corresponds to the interlayer distance of the (100) planes of La_2O_3 crystals (inset in Figure 1i).

This wet-chemistry route relies on a tamed precipitation of La^{3+} and is readily applicable for the surface treatment of a large variety of seed materials (Figure S3), particularly NLO powder. Taking single crystalline $LiNi_{0.83}Co_{0.07}Mn_{0.1}O_2$ (NCM0.83) as an example, we investigated its morphological change before and after $La(OH)_3$ formation. The pristine NCM0.83 seeds are highly crystalline particles with a clean surface borderline (Figure 1j). After a typical DIP process as depicted in the experimental section, an $La(OH)_3$ nanoshell emerged without causing noticeable damage on the neighboring lattices of NCM0.83 (inset in Figure 1k). The high uniformity and ultrathin thickness of this 2 nm conformal coating (Figure 1k) manifested a comparable capability to a typical ALD technique but depends on a more flexible and low-cost process through the solution-based reaction. Furthermore, different nanoshells with thickness controlled at 5, 8, and 30 nm, respectively, were prepared as shown in Figure 1l−n by varying the NCM0.83 amounts. The distribution of chemical components was also investigated by the EDS mapping (Figure 1o) of the NCM0.83 particles, which disclosed a homogeneous distribution of the La species in the surface nanoshells.

Due to the unstable nature of NCM0.83 materials, the previous construction of precisely defined nanoshells unexceptionally relies on vapor-based techniques. Our synthesis design revealed the high potential of a wet-chemistry route to conceivably replace the ALD technique, which endowed us with a versatile tool to build a model system for a systematic investigation of the surface chemistry of this representative NLO cathode for performance optimization. Interestingly, a quick electrochemical characterization showed that the introduction of a chemically inert shell, particularly 5 nm $La(OH)_3$ (denoted as NCM@5La), would cause an immediate decrease of the reversible capacity to 183.4 mAh g^{-1} from 195.7 mAh g^{-1} of the pristine NCM0.83 at 0.1 C (1 C = 200 mAh g^{-1}) between 3.0 and 4.3 V (Figure S4). The associated high interface resistance revealed that a thick and conformal coating that is not Li^+ conductive was detrimental to charge transportation and easily caused adverse effects on the battery performance. As discussed in details later in this work, we were able to circumvent this dilemma by initiating a solid reaction

https://doi.org/10.1021/jacs.2c13787
J. Am. Chem. Soc. 2023, 145, 7397−7407

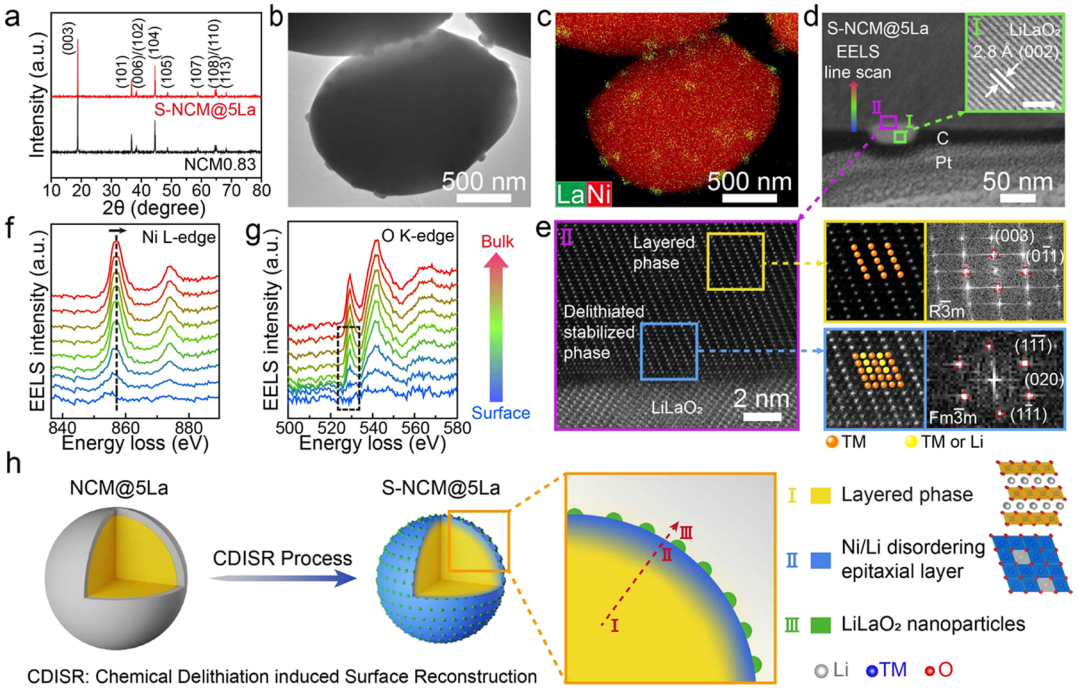

Figure 2. Design and surface characterization of S-NCM@5La after heat treatment. (a) XRD spectra of NCM0.83 and S-NCM@5La. TEM image (b) and corresponding elemental mapping (c) of the S-NCM@5La sample. (d) Low-magnification STEM image of a partial cross-sectional slice of S-NCM@5La particle prepared by focused ion beam (FIB). From up to down are S-NCM@5La particle including the NCM0.83 substrate and La-enriched islands, C films, and Pt films, respectively. The inset is the HRTEM image in the green square I, which shows a lattice spacing of 2.8 Å for the $LiLaO_2$ (002) planes. (e) HAADF−STEM image of the purplish red square II in Figure 2d; magnified HAADF−STEM and corresponding reduced fast Fourier transform (FFT) image of the selected area (yellow and blue square). (f,g) EELS spectra of the Ni L-edges (f) and O K-edges (g) extracted from the surface to the inside region (colored line in Figure 2d). (h) Schematic illustration of the surface lattice modulation process and the structural features of the formed S-NCM@5La.

between $La(OH)_3$ coating and its neighboring NCM0.83 lattices through an optimized sintering process at 750 °C, which transformed the flimsy surface into a favorable structure to ensure both high cycling stability and high rate capability.

Systematic characterizations were conducted to probe the subtle change of the NCM@5La sample in response to the surface solid reaction. For the sintered sample (denoted as S-NCM@5La), its XRD pattern showed almost identical peaks to the unmodified powders (Figure 2a), indicating that the surface transition did not cause noticeable change in the crystalline structure of the bulk. The elemental analysis by using inductively coupled plasma-mass spectrometry (ICP-MS) showed that the amount of La was 0.25 at % in S-NCM@5La (Table S1). A careful TEM analysis revealed the disappearance of the characteristic core−shell-type configuration while tiny nanoparticles with a diameter below 100 nm emerged to decorate the micro-sized particles (Figure 2b). The EDS elemental mapping (Figures 2c and S5) of a representative S-NCM@5La particle manifested that the surface islands consisted of mainly La species, and there existed hardly any La signal detectable from the micro-sized support, which were the NCM0.83 particles having a uniform distribution of Ni, Co, and Mn. It is therefore expected that the heat treatment caused a rupture and transformed the previous shell into small-sized nanoparticles on the NCM0.83 particles.

Scanning transmission electron microscopy (STEM) combined with electron energy loss spectroscopy (EELS) was used to explore the surface structure at atomic resolution (Figure 2d−g). First, the micro-sized particle was cross-sectioned by the focused ion beam (FIB) milling technique, whose operation mainly includes the sequential deposition of both C and Pt films on the sample to alleviate the destruction from the Ga-ion beam and the following ion milling to prepare a thin slice with a thickness below 100 nm. Figure 1d shows a typical STEM image of the cross-sectional sample with the NCM0.83 substrate, the La-enriched islands, as well as the protective films of both carbon and Pt. This newly formed nanoparticle was highly crystalline with an interplanar spacing of 2.8 Å, which could be well indexed to the (002) plane of the monoclinic $LiLaO_2$. The aberration-corrected STEM operated under a high-angle annular dark-field (HAADF) mode was used to study the lattice characters of the cathode material. As shown in Figure 2e, the HAADF−STEM image showed that $LiLaO_2$ nanoparticles contacted closely with their substrates, and there existed no discernible gap in between. Interestingly, although the inner part of the NCM0.83 microparticle maintained a characteristic layer structure as displayed in the yellow square, a close look at the outer margin of the microparticle revealed a slight transition of the lattice structure. Specifically, the TM slabs remained unchanged as continuous arrays of white dots, but there emerged TM signals as highlighted in the blue square from the Li slabs right on the surface, showing a Ni/Li disordering structure (blue square) with a depth of around 3 nm as an epitaxial layer. The right panel in Figure 2e shows magnified images of these two involved lattices as well as results from their reduced FFT analysis. We also applied the spatially resolved STEM−EELS technique to study the difference of the chemical environment associated with this phase transition. A line-scan EELS was performed to collect the data from the surface to the bulk in a

https://doi.org/10.1021/jacs.2c13787
J. Am. Chem. Soc. 2023, 145, 7397−7407

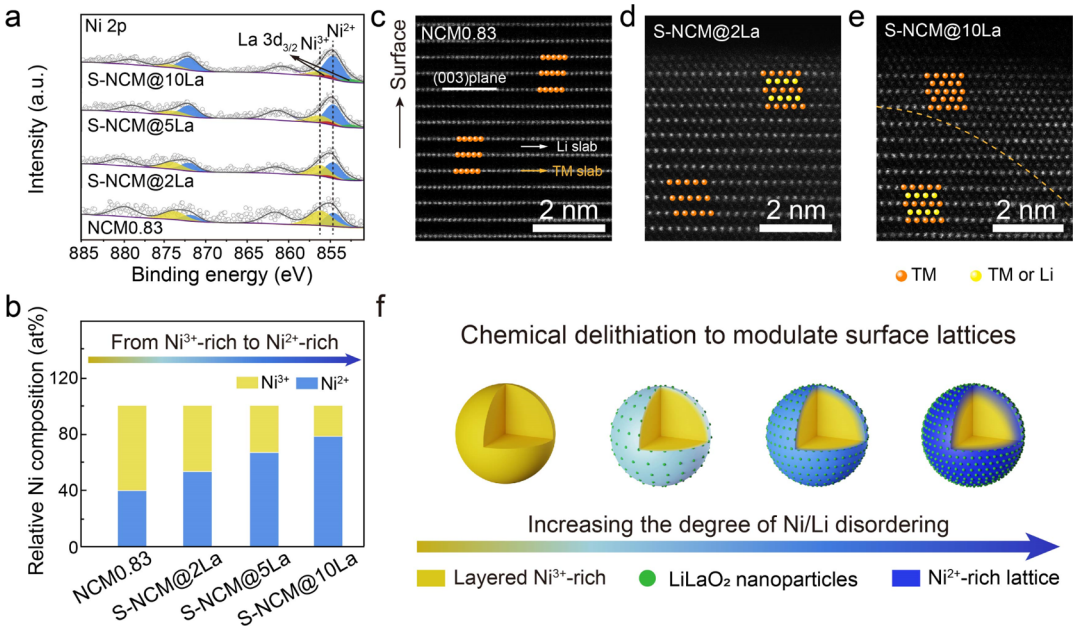

Figure 3. Surface lattice modulation and characterization of samples with different La amounts. (a) XPS characterization of Ni 2p peaks of samples with different La amounts, (b) relative composition of Ni on the surface as a function of La amount. HAADF−STEM images of the sample surface with increasing La amount: NCM0.83 (c), S-NCM@2La (d), S-NCM@10La (e). (f) Schematic illustration of the structural evolution of the NLO surface in response to a gradually escalated delithiation effect.

direction marked by the colored arrow in Figure 2d. The in-depth analysis of the Mn L-edge and Co L-edge signals (Figure S6a,b) showed no obvious change, indicating that these two elements kept their valence unchanged at different locations.[36] As a sharp contrast, the surface-to-bulk profiles of the Ni L_3-edge demonstrated a progressive shift toward higher energy, revealing that the surface Ni species existed mainly in a Ni^{2+}-rich type when compared to the Ni^{3+}-dominating inner core (Figure 2f). Such a Ni^{2+}-rich structure has been verified to help enhance the structural and interfacial stability of the NLO cathode.[37,38] Meanwhile, the weak intensity of the pre-edge peak in O K-edge spectra unveiled the existence of oxygen vacancies on the surface (Figure 2g). Notably, our detailed STEM−EELS analysis found that the reconstructed NCM0.83 microparticle itself did not exhibit La signal on its surface, revealing that the La species had been mainly sintered into the outmost $LiLaO_2$ islands rather than doped into the NCM0.83 lattice (Figure S6c).

The analysis of the local features of the S-NCM@5La sample unfolded a heated-induced solid reaction between the $La(OH)_3$ and the NCM0.83 surface lattice, leading to the formation of $LiLaO_2$ nanoparticles and a simultaneous lattice reconstruction in the crust of the NCM0.83 particles. Due to the technical challenge, an accurate image to describe the atomic reconstruction during the solid-state reaction was currently not possible. We speculated that the structural stabilization includes at least two processes in view of our observations of the surface chemicals. First, the oxidation of lattice oxygen was expected as revealed by the emergence of abundant oxygen vacancies on the particle surface, which is probably related to the delithiation of surface Li^+ during the high-temperature reaction, and accordingly initiated the transition to Ni^{2+}.[39] Second, the occupation of the Li^+ site by Ni^{2+} due to the similarity of the ionic radius of Li^+ (0.76 Å) and Ni^{2+}(0.69 Å), which leads to a widely reported process known as Li^+/Ni^{2+} mixing,[40] formed a Ni/Li disordering structure. The hypothesized chemical reactions are shown in the Supporting Information (eqs S1−S5). A summary of the structural features of the formed S-NCM@5La is depicted in Figure 2h, where reconstructed surface lattices are described in blue color to differentiate from the inner layered structure, while $LiLaO_2$ particles are depicted in green color to decorate the NCM0.83 substrate.

Considering that the Ni/Li disordering structure has been previously observed by different groups during the pursuit to stabilize NLO cathode materials through commonly doping treatments,[41] it raised our concerns about its function since it may seem counterintuitive in view of the fact that such a structure could be detrimental to the NLO material due to its inert nature. Fortunately, the surface solid reaction endowed us with a flexible tool to modulate the surface chemistry by taking full advantage of our synthesis capability in building uniform nanoshells for the following chemical delithiation process. In this regard, we studied two other samples denoted as S-NCM@2La and S-NCM@10La, respectively, as differentiated by the nanoshells built for the delithiation reaction. The chemical compositions of these cathodes are shown in Table S1 through ICP-MS analysis. In view of the high sensitivity of Ni species to the surface reconstruction as well as its significant impact on the electrochemical behavior, X-ray photoelectron spectroscopy (XPS) analysis (Figure 3a) was carried out to compare the valence of surface Ni species with a detection depth around 5 nm. The signals for Ni^{2+} (854.9 eV) and Ni^{3+} (856.0 eV) were deconvoluted from the Ni $2p_{1/2}$ spectra,[42] and roughly calculated results of their atomic percentage are plotted in Figure 3b, which shows a continuous increase of Ni^{2+} content on the surface along with the increment of delithiation. The surface reactions were efficient to create a Ni^{2+}-rich surface but meanwhile preserved a certain amount of reactive Ni^{3+}, which reduced the risk of forming a rock-salt phase like NiO to lose Li^+ conductivity. HAADF−STEM images were recorded to reveal the surface structure of NCM

https://doi.org/10.1021/jacs.2c13787
J. Am. Chem. Soc. 2023, 145, 7397−7407

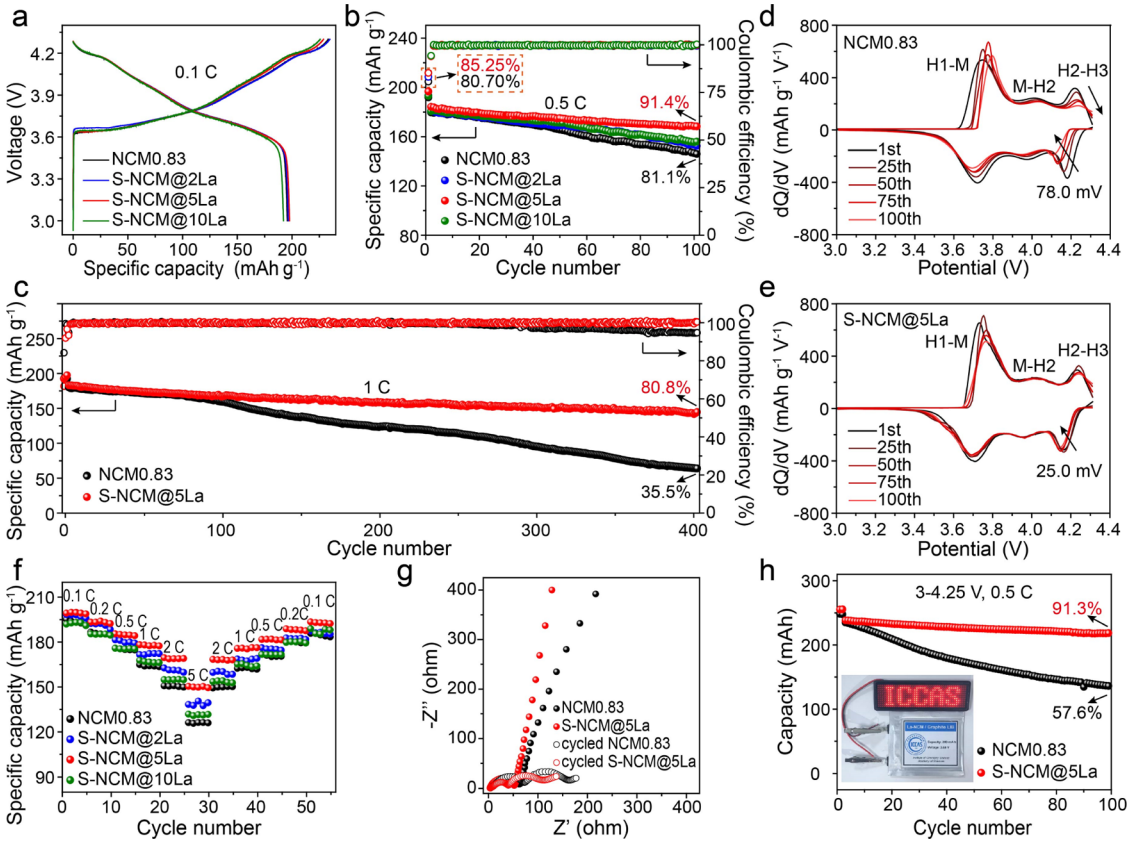

Figure 4. Electrochemical characterization of surface-controlled samples. (a) Charge−discharge profiles during the first cycle at 0.1 C (1 C = 200 mAh g^{-1}) for 3.0−4.3 V. Cycling performance at 0.5 C (b) and 1 C (c) for 3.0−4.3 V. dQ/dV profiles during cycling for NCM0.83 (d) and S-NCM@5La (e). (f) Rate performance. (g) EIS spectra of NCM0.83 and S-NCM@5La before cycling and after 100 cycles at 0.1 C. (h) Cycling performance of NCM and S-NCM@5La/graphite full cells at 0.5 C within 3.0−4.25 V. Inset is the digital image of the assembled pouch cell (Institute of Chemistry, Chinese Academy of Sciences badge: permission for use obtained from the Institute of Chemistry, Chinese Academy of Sciences).

samples (Figure 3c−e). The pristine NCM0.83 showed a well-defined layered symmetry on the surface. As for S-NCM@2La, it started to experience slight lattice transition within a depth of below 2 nm as revealed by the weak signal of white dots from the Li^+ 3a sites (Figure 3d). Such a lattice transition became prominent for S-NCM@10La with an obviously higher Ni^{2+}-occupation ratio in Li slabs (Figure 3e) over a wider area below the surface. Our further XRD analysis confirmed that the bulk phase did not experience noticeable transformation of its layered structure (Figure S7). However, the Rietveld refinement of the XRD patterns (Figure S8 and Table S2) showed slightly increased values of different lattice parameters such as the a-axis, c-axis, and the unit cell volume upon a higher degree of chemical delithiation on the surface, likely owing to the relatively larger ionic radius of Ni^{2+} (0.69 Å) than Ni^{3+} (0.60 Å). The continuous structural transformation is schemed in Figure 3f, which describes an increased degree of lattice reconstruction through Ni/Li disordering in response to chemical delithiation of the surface. Such a reaction-dependent surface property not only implies their complicated nature for structure-performance investigation but also highlights the importance of nanoshell control to achieve a reliable description of the local structures of cathode materials.

Inspired by the essential role played by the surface chemistry in the structural and electrochemical stability of high energy cathode, we carried out a systematic evaluation of battery performance on these surface-modulated NCM0.83 samples. Figure 4a compares the first charge/discharge curves of the different samples tested at 0.1 C in 3.0−4.3 V. All the samples after solid state reaction exhibited electrochemical profiles almost identical to that of pristine NCM0.83, revealing that the surface treatment did not have a substantial impact on the Li^+-storage behavior, which rewarded our elaborate synthesis design based on a solution-based route for precise surface control. Further cycling test showed that the cycling performance was closely related to surface properties (Figure 4b). After 100 cycles at 0.5 C, the NCM0.83 electrode showed a capacity retention of only 81.1%, showcasing the inevitable capacity fading for a typical NLO cathode. We found that the S-NCM@2La sample featuring a slight surface lattice reconstruction was able to improve the capacity retention capability to 84.4%. Notably, the surface control endowed the S-NCM@5La electrode with a capability to retain as high as 91.4% of its initial capacity after 100 cycles. However, a high content of rock-salt-like phase on the constructed surface as observed on S-NCM@10La became detrimental to the reversible capacity (Figure 4a) and less beneficial to the cycling stability (86.3%), and it would cause significant damage to the battery performance when far thicker nanoshells were used for surface reconstruction (Figure S9). The electrochemical test identified S-NCM@5La as an optimized cathode material. Figure 4c compares a representative long cycle test at 1 C, where an outstanding enhancement in capacity retention (from 35.5 to 80.8% after 400 cycles) was achieved upon surface engineering.

https://doi.org/10.1021/jacs.2c13787
J. Am. Chem. Soc. 2023, 145, 7397−7407

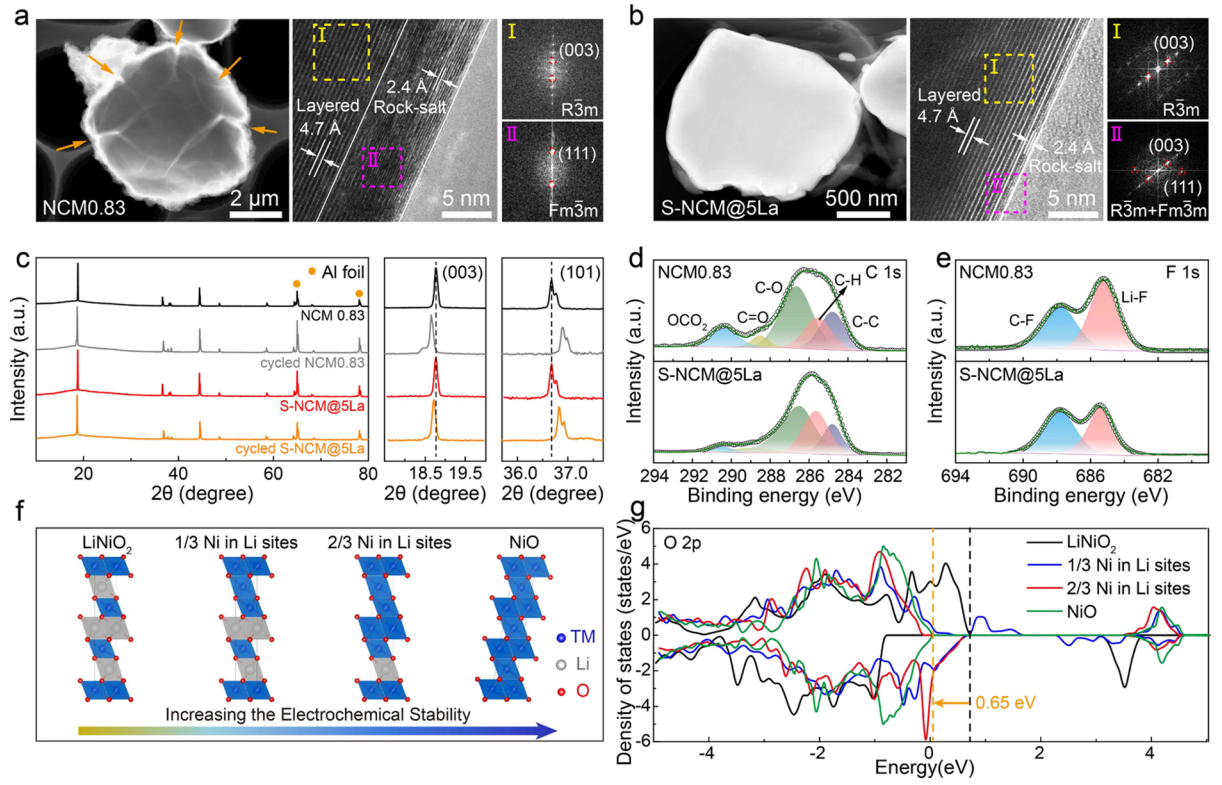

Figure 5. Structural and interfacial stability after cycling. Dark-field TEM, HRTEM image, and corresponding FFT of the interesting area of 100 cycled NCM0.83 (a) and S-NCM@5La (b) at 0.1 C. (c) XRD patterns of NCM0.83 and S-NCM@5La before and after cycling. C 1s (d) and F 1s (e) XPS spectra of cycled NCM0.83 and S-NCM@5La. (f) Atomic models of $LiNiO_2$, 1/3, 2/3, and all of the Li sites substituted by Ni^{2+} ions. The blue, sliver, and red balls represent the TM, Li, and O atoms, respectively. (g) Corresponding 2p projected density of states of O in these models. The Fermi level was shifted to zero. (The VBM was shifted by about 0.64 eV from $LiNiO_2$ to NiO).

To better understand the degradation behavior, the differential capacity (dQ/dV) analysis was carried out on these two electrodes (Figure 4d,e) with special attention paid to the H2−H3 phase transition at around 4.2 V, which has been widely recognized to be responsible for the lattice distortion in the *c*-axis, thus reflecting the structural stability.[43] During the cycling, the dQ/dV peak at 4.2 V of the NCM0.83 cathode continuously shifted to a lower voltage direction and reached a decreased value of 78.0 mV along with a much-reduced peak intensity, featuring a high polarization process which showed irreversible phase degradation of the cathode material to experience continuous loss of activity. In sharp contrast, the S-NCM@5La sample showed a smaller change in peak shift of 25.0 mV and an almost constant peak intensity in the dQ/dV profile, which explained well a much-favored structural stability to maintain reversible H2−H3 transition for extended cycles.

It was found that the surface lattice modulation is able to boost the rate capability of this high energy NLO cathode. Typically, the S-NCM@5La cathode delivered a high reversible capacity of 144.2 mAh g^{-1} at a high rate of 5 C, showing an increase of 23.9% when compared to 116.4 mAh g^{-1} delivered by the NCM0.83 one (Figure 4f). Although a pure rock-salt structure where nickel species existed as Ni^{2+}, for example, in the case of NiO, has been widely recognized as an inert phase detrimental to the battery performance, and the agglomerated $LiLaO_2$ particles may be harmful for Li^+ conduction (Figure S10), our surface modulation revealed the possibility to achieve a balanced effect by forming a Ni^{2+}-rich lattice with a suitable preservation of Ni^{3+} and small ionic conducting $LiLaO_2$ nanoparticles to facilitate Li^+ transfer, which could be facilely achieved by adjusting the surface $La(OH)_3$ content to control the degree of chemical delithiation. Meanwhile, the $LiLaO_2$ nanoparticles coherently share the lattices with the NCM0.83 substrate on the borderline (Figure 2e), which is also beneficial to the kinetics of Li^+ transportation. The galvanostatic intermittent titration technique (GITT) measurement showed the increased D_{Li}^+ of S-NCM@5La compared with the pristine NCM0.83, indicating the enhanced diffusion capability which determines the kinetics of the charge/discharge process, thus achieving superior rate performance (Figure S11).[44,45] As the surface delithiation went deeper, and the Ni^{2+} tended to dominate the surface, a much-deteriorated rate performance of the S-NCM@20La electrode was observed (Figure S12), reflecting not only the deleterious nature of the deep-delithiated structure in jeopardizing Li^+ transfer but also the essential role of lattice modulation to satisfy the need in both cyclability and rate capability. Electrochemical impedance spectroscopy (EIS) was then used to probe the cathode−electrolyte interface during the cycling (Figures 4g and S13). The charge transfer resistance (R_{ct}) increased from 51.5 to 104.4 Ω after 100 cycles, which indicated a deteriorated interface probably related to structural degradation and side reactions. In contrast, the surface-reconstructed S-NCM@5La cathode showed much reduced R_{ct} either before (44.7 Ω) or after (80.0 Ω) 100 cycles, evidencing a stable CEI for fast charge transfer, which meanwhile explains well its substantially improved cycling capability.

The advantage of surface lattice modulation on the NLO materials was further studied by the electrochemical test on a

https://doi.org/10.1021/jacs.2c13787
J. Am. Chem. Soc. 2023, 145, 7397−7407

pouch cell assembled by S-NCM@5La and a graphite anode. We did observe an obvious boost of the cycling capability with a capacity retention of 91.3% after 100 cycles, a value much higher than 57.6% of the pristine NCM0.83 when tested at 0.5 C, which promised high potential of our control strategy for the practical application of the NLO cathode materials in LIBs (Figure 2h).

Encouraged by the obvious advantage of surface lattice control, further characterizations were conducted to have a better understanding of the stabilization mechanism of the prepared cathodes. It was found that the surface modification was very effective to prevent the formation of microcracks in the NCM0.83 cathode materials, which ensures its good structural stability to sustain long cycles. For the cathodes tested after 100 cycles at 0.1 C, the unmodified sample of NCM0.83 suffered from severe mechanical damage with microcracks all over the particle as revealed by the dark-field TEM analysis in Figure 5a. The emergence of microcracks has been widely acknowledged as a result of internal strains and stress during extended cycling. As for the single crystals of NLO particles, their cracking would further aggravate their parasitic reaction with electrolytes penetrating the internal parts of the cathode particles and then exacerbate the capacity fading. The HRTEM analysis of the cycled NCM0.83 particles showed that the surface was susceptible to a microstructural transformation to form a pure NiO structure, while a serious dissolution of TMs was disclosed by the ICP-MS test (Table S3), which manifested the irreversible structural degradation during the electrochemical process. In sharp contrast, the cycled S-NCM@5La particle maintained an integrated structure with no microcracks (Figure 5b) detected by the dark-field TEM analysis. The surface also remained almost intact with a successfully diminished structural transformation to the detrimental NiO phase. The ICP-MS tests confirmed that the surface modification could greatly suppress TM dissolution during cycling (Table S3), which conveyed an additional benefit by avoiding the deposition of dissolved TMs on the anode electrode and uncontrollable growth of the solid−electrolyte interphase (SEI), thus maintaining the interfacial properties and improving the full-cell cycling stability (Figure S14). Benefiting from our synthesis that produced a uniform and ultrathin epitaxial layer on the NLO particle surface, the lithiation/delithiation inhomogeneity could be will eliminated, thus effectively propagating the structure degradation during cycling. The structural changes of the cycled NCM0.83 and S-NCM@5La were identified by XRD patterns (Figure 5c). The stronger diffraction intensities of S-NCM@5La than that of untreated NCM0.83 implied the less destructed bulk structure of the surface reconstructed one. Besides, the corresponding magnified regions showed both much mitigated left-shift (003) peak and right-shift (101) peak of the cycled S-NCM@5La sample compared to the unmodified one, indicating that the structural stability of the material can be maintained after our surface treatment. The XPS analysis was also used to characterize the near-surface chemical compositions of the cycled samples (Figures 5d,e and S15). It turned out that a much weaker intensity of LiF signal was recorded for S-NCM@5La when compared to that of NCM0.83, which implied a much-reduced $LiPF_6$ electrolyte decomposition due to the surface treatment.[46] Moreover, the relatively weaker intensities of the C−O, C═O, and OCO_2 peaks of S-NCM@5La also implied a lower carbonate electrolyte decomposition amount after modification.[43] Our XPS results identified that the modified surface showed improved stability with much-reduced electrode/electrolyte side reactions, which could protect the bulk structure from continuous TM loss, considering the fact that its diffusion across the particle was accelerated by concentration gradient.

To understand such a favored surface chemistry in combating side reactions, density functional theory (DFT) calculation was used to probe the density of state (DOS) of the concerned samples, which has been widely used as an indicator to measure surface activity.[47,48] The structure with the $R\bar{3}m$ space group was adopted for the calculations based on the space group of layered $LiNiO_2$, where different degrees of Li/Ni cation mixing were studied to investigate their surface activities (Figure 5f). As shown in Figure 5g, substituting 1/3 Li ions with Ni^{2+} in $LiNiO_2$ was able to lower the O p band with respect to the Fermi level, and the increase of Ni^{2+} occupation would further downshift the O p band. Such a ligand p-band downward shift indicated a higher energy barrier for electron transfer from the electrolyte, resulting in inhibited electrolyte oxidation by dehydrogenation.[47] The DOS analysis also showed that the NiO structure possessed the lowest O p band and probably displayed the most inert nature against electrolyte oxidation. However, the poor Li^+ conductivity of this structure made it inferior to act as a uniform coating for the surface treatment of cathode materials. Therefore, by modulating the ratio of Ni in the Li site, for example, chemical delithiation-induced surface transition, a favorable balance could be achieved on the surface lattice to ensure both high electrochemical stability and fast charge transfer.

CONCLUSIONS

In summary, the possibility to stabilize the high-energy NLO cathode was demonstrated through a direct modulation of its surface lattices, whose reconstruction through Ni/Li disordering could successfully reverse its unstable nature, thereby becoming highly efficient to combat side reactions and chemophysical degradation. To achieve a clear description of the surface change, we managed to build $La(OH)_3$ coatings with nanometer precision, which experienced a solid reaction with the NCM0.83 surface in a controlled manner upon sintering at a high temperature, accordingly introducing a favorable degree of Ni/Li disordering in the NCM0.83 crust with a substantially reduced oxidative Ni^{3+}. Our experimental and theoretical calculations showed that the reconstructed surface showed much lower reactivity with organic electrolytes and was efficient to suppress the parasitic reactions on the cathode−electrolyte interface. Notably, such a fortified lattice combined with the formed $LiLaO_2$ on the NCM0.83 surface showed an extraordinary capability to not only mitigate its painstaking irreversible phase transformation but also make the NCM0.83 particle mechanically stable against cracking, thereby ensuring a significantly improved cycling capability (80.8% after 400 cycles at 1 C compared to 35.5% of the control sample) and excellent rate performance (144.2 mAh g^{-1} at 5 C while 116.4 mAh g^{-1} for the control sample). Our work discloses the sensitive nature of the surface reaction between the nanocoating and its underneath NLO lattices during the sintering treatment and provides a new research avenue to build inherently stable cathode materials through their surface lattice modulation for reliable and high-energy LIBs.

https://doi.org/10.1021/jacs.2c13787
J. Am. Chem. Soc. 2023, 145, 7397−7407

■ ASSOCIATED CONTENT

Supporting Information

The Supporting Information is available free of charge at https://pubs.acs.org/doi/10.1021/jacs.2c13787.

Details of preparations, characterizations, electrochemical tests, and calculations and additional TEM, XRD, electrochemical performance curves, EDS, EELS, GITT, EIS, SEM, and XPS (PDF)

■ AUTHOR INFORMATION

Corresponding Authors

An-Min Cao − *CAS Key Laboratory of Molecular Nanostructure and Nanotechnology, and Beijing National Laboratory for Molecular Sciences, Institute of Chemistry, Chinese Academy of Sciences (CAS), Beijing 100190, P. R. China; University of Chinese Academy of Sciences, Beijing 100049, P. R. China;* orcid.org/0000-0001-9280-4337; Email: anmin_cao@iccas.ac.cn

Li-Jun Wan − *CAS Key Laboratory of Molecular Nanostructure and Nanotechnology, and Beijing National Laboratory for Molecular Sciences, Institute of Chemistry, Chinese Academy of Sciences (CAS), Beijing 100190, P. R. China; University of Chinese Academy of Sciences, Beijing 100049, P. R. China;* orcid.org/0000-0002-0656-0936; Email: wanlijun@iccas.ac.cn

Authors

Si-Qi Lu − *CAS Key Laboratory of Molecular Nanostructure and Nanotechnology, and Beijing National Laboratory for Molecular Sciences, Institute of Chemistry, Chinese Academy of Sciences (CAS), Beijing 100190, P. R. China; University of Chinese Academy of Sciences, Beijing 100049, P. R. China*

Qinghua Zhang − *Beijing National Laboratory for Condensed Matter Physics, Institute of Physics, Chinese Academy of Sciences (CAS), Beijing 100190, P. R. China*

Fanqi Meng − *University of Chinese Academy of Sciences, Beijing 100049, P. R. China; Beijing National Laboratory for Condensed Matter Physics, Institute of Physics, Chinese Academy of Sciences (CAS), Beijing 100190, P. R. China*

Ya-Ning Liu − *College of Materials Science and Engineering, Zhejiang University of Technology, Hangzhou 310014, China*

Jianjun Mao − *Department of Chemistry, The University of Hong Kong, Hong Kong 999077, P. R. China; Hong Kong Quantum AI Lab Limited, Hong Kong 999077, P. R. China;* orcid.org/0000-0003-2265-9685

Sijie Guo − *CAS Key Laboratory of Molecular Nanostructure and Nanotechnology, and Beijing National Laboratory for Molecular Sciences, Institute of Chemistry, Chinese Academy of Sciences (CAS), Beijing 100190, P. R. China*

Mu-Yao Qi − *CAS Key Laboratory of Molecular Nanostructure and Nanotechnology, and Beijing National Laboratory for Molecular Sciences, Institute of Chemistry, Chinese Academy of Sciences (CAS), Beijing 100190, P. R. China; University of Chinese Academy of Sciences, Beijing 100049, P. R. China*

Yan-Song Xu − *CAS Key Laboratory of Molecular Nanostructure and Nanotechnology, and Beijing National Laboratory for Molecular Sciences, Institute of Chemistry, Chinese Academy of Sciences (CAS), Beijing 100190, P. R. China; Department of Chemistry, College of Science, Huazhong Agricultural University, Wuhan 430070, P. R. China*

Yan Qiao − *University of Chinese Academy of Sciences, Beijing 100049, P. R. China; Beijing National Laboratory for Molecular Sciences (BNLMS), Laboratory of Polymer Physics and Chemistry, CAS Research/Education Center for Excellence in Molecular Sciences, Institute of Chemistry, Chinese Academy of Sciences, Beijing 100190, China;* orcid.org/0000-0003-1069-7756

Si-Dong Zhang − *CAS Key Laboratory of Molecular Nanostructure and Nanotechnology, and Beijing National Laboratory for Molecular Sciences, Institute of Chemistry, Chinese Academy of Sciences (CAS), Beijing 100190, P. R. China; University of Chinese Academy of Sciences, Beijing 100049, P. R. China*

Kecheng Jiang − *Dongguan TAFEL New Energy Technology Company, Limited, Dongguan 523000, P. R. China*

Lin Gu − *School of Materials Science and Engineering, Tsinghua University, Beijing 100084, China*

Yang Xia − *College of Materials Science and Engineering, Zhejiang University of Technology, Hangzhou 310014, China;* orcid.org/0000-0001-9627-4898

Shuguang Chen − *Department of Chemistry, The University of Hong Kong, Hong Kong 999077, P. R. China; Hong Kong Quantum AI Lab Limited, Hong Kong 999077, P. R. China*

GuanHua Chen − *Department of Chemistry, The University of Hong Kong, Hong Kong 999077, P. R. China; Hong Kong Quantum AI Lab Limited, Hong Kong 999077, P. R. China;* orcid.org/0000-0001-5015-0902

Complete contact information is available at: https://pubs.acs.org/10.1021/jacs.2c13787

Notes

The authors declare no competing financial interest.

■ ACKNOWLEDGMENTS

This work was supported by the National Key R&D Program of China (Grant No. 2022YFB2404402), the National Natural Science Foundation of China (Grant Nos. 22025507 and 21931012), the Key Research Program of Frontier Sciences, CAS (ZDBS-LYSLH020), the innovation team for R&D and industrialization of High Energy Density Si-Based Power batteries (Item No. 2018607219003), and the Beijing National Laboratory for Molecular Sciences (BNLMS-CXXM-202010). We thank Jing Tai and Bo Guan from the Center for Physiochemical Analysis and Measurement in the Institute of Chemistry (CAS) for assisting with EDS mapping analysis.

■ REFERENCES

(1) Goodenough, J. B.; Park, K.-S. The Li-Ion Rechargeable Battery: A Perspective. *J. Am. Chem. Soc.* **2013**, *135*, 1167−1176.

(2) Choi, J. W.; Aurbach, D. Promise and reality of post-lithium-ion batteries with high energy densities. *Nat. Rev. Mater.* **2016**, *1*, 16013.

(3) Lee, J.; Urban, A.; Li, X.; Su, D.; Hautier, G.; Ceder, G. Unlocking the Potential of Cation-Disordered Oxides for Rechargeable Lithium Batteries. *Science* **2014**, *343*, 519−522.

(4) Pomerantseva, E.; Bonaccorso, F.; Feng, X.; Cui, Y.; Gogotsi, Y. Energy storage: The future enabled by nanomaterials. *Science* **2019**, *366*, No. eaan8285.

(5) Lu, J.; Chen, Z.; Ma, Z.; Pan, F.; Curtiss, L. A.; Amine, K. The role of nanotechnology in the development of battery materials for electric vehicles. *Nat. Nanotechnol.* **2016**, *11*, 1031−1038.

(6) Li, W.; Erickson, E. M.; Manthiram, A. High-nickel layered oxide cathodes for lithium-based automotive batteries. *Nat. Energy* **2020**, *5*, 26−34.
(7) Xue, W.; Huang, M.; Li, Y.; Zhu, Y. G.; Gao, R.; Xiao, X.; Zhang, W.; Li, S.; Xu, G.; Yu, Y.; Li, P.; Lopez, J.; Yu, D.; Dong, Y.; Fan, W.; Shi, Z.; Xiong, R.; Sun, C.-J.; Hwang, I.; Lee, W.-K.; Shao-Horn, Y.; Johnson, J. A.; Li, J. Ultra-high-voltage Ni-rich layered cathodes in practical Li metal batteries enabled by a sulfonamide-based electrolyte. *Nat. Energy* **2021**, *6*, 495−505.
(8) Schmuch, R.; Wagner, R.; Hörpel, G.; Placke, T.; Winter, M. Performance and cost of materials for lithium-based rechargeable automotive batteries. *Nat. Energy* **2018**, *3*, 267−278.
(9) Li, J.; Sharma, N.; Jiang, Z.; Yang, Y.; Monaco, F.; Xu, Z.; Hou, D.; Ratner, D.; Pianetta, P.; Cloetens, P.; Lin, F.; Zhao, K.; Liu, Y. Dynamics of particle network in composite battery cathodes. *Science* **2022**, *376*, 517−521.
(10) Xu, C.; Märker, K.; Lee, J.; Mahadevegowda, A.; Reeves, P. J.; Day, S. J.; Groh, M. F.; Emge, S. P.; Ducati, C.; Layla Mehdi, B.; Tang, C. C.; Grey, C. P. Bulk fatigue induced by surface reconstruction in layered Ni-rich cathodes for Li-ion batteries. *Nat. Mater.* **2021**, *20*, 84−92.
(11) Zhang, H.; Wang, L.; He, X. Trends in a study on thermal runaway mechanism of lithium-ion battery with LiNixMnyCo1-x-yO2 cathode materials. *Battery Energy* **2022**, *1*, 20210011.
(12) Liu, T.; Yu, L.; Lu, J.; Zhou, T.; Huang, X.; Cai, Z.; Dai, A.; Gim, J.; Ren, Y.; Xiao, X.; Holt, M. V.; Chu, Y. S.; Arslan, I.; Wen, J.; Amine, K. Rational design of mechanically robust Ni-rich cathode materials via concentration gradient strategy. *Nat. Commun.* **2021**, *12*, 6024.
(13) Lin, F.; Nordlund, D.; Li, Y.; Quan, M. K.; Cheng, L.; Weng, T.-C.; Liu, Y.; Xin, H. L.; Doeff, M. M. Metal segregation in hierarchically structured cathode materials for high-energy lithium batteries. *Nat. Energy* **2016**, *1*, 15004.
(14) Li, W.; Dolocan, A.; Oh, P.; Celio, H.; Park, S.; Cho, J.; Manthiram, A. Dynamic behaviour of interphases and its implication on high-energy-density cathode materials in lithium-ion batteries. *Nat. Commun.* **2017**, *8*, 14589.
(15) Romano Brandt, L.; Marie, J.-J.; Moxham, T.; Förstermann, D. P.; Salvati, E.; Besnard, C.; Papadaki, C.; Wang, Z.; Bruce, P. G.; Korsunsky, A. M. Synchrotron X-ray quantitative evaluation of transient deformation and damage phenomena in a single nickel-rich cathode particle. *Energy Environ. Sci.* **2020**, *13*, 3556−3566.
(16) Xu, Z.; Jiang, Z.; Kuai, C.; Xu, R.; Qin, C.; Zhang, Y.; Rahman, M. M.; Wei, C.; Nordlund, D.; Sun, C.-J.; Xiao, X.; Du, X.-W.; Zhao, K.; Yan, P.; Liu, Y.; Lin, F. Charge distribution guided by grain crystallographic orientations in polycrystalline battery materials. *Nat. Commun.* **2020**, *11*, 83.
(17) Ou, X.; Liu, T.; Zhong, W.; Fan, X.; Guo, X.; Huang, X.; Cao, L.; Hu, J.; Zhang, B.; Chu, Y. S.; Hu, G.; Lin, Z.; Dahbi, M.; Alami, J.; Amine, K.; Yang, C.; Lu, J. Enabling high energy lithium metal batteries via single-crystal Ni-rich cathode material co-doping strategy. *Nat. Commun.* **2022**, *13*, 2319.
(18) Yan, P.; Zheng, J.; Gu, M.; Xiao, J.; Zhang, J.-G.; Wang, C.-M. Intragranular cracking as a critical barrier for high-voltage usage of layer-structured cathode for lithium-ion batteries. *Nat. Commun.* **2017**, *8*, 14101.
(19) Bi, Y.; Tao, J.; Wu, Y.; Li, L.; Xu, Y.; Hu, E.; Wu, B.; Hu, J.; Wang, C.; Zhang, J. G.; Qi, Y.; Xiao, J. Reversible planar gliding and microcracking in a single-crystalline Ni-rich cathode. *Science* **2020**, *370*, 1313−1317.
(20) Yu, H.; Cao, Y.; Chen, L.; Hu, Y.; Duan, X.; Dai, S.; Li, C.; Jiang, H. Surface enrichment and diffusion enabling gradient-doping and coating of Ni-rich cathode toward Li-ion batteries. *Nat. Commun.* **2021**, *12*, 4564.
(21) Lee, W.; Muhammad, S.; Sergey, C.; Lee, H.; Yoon, J.; Kang, Y.-M.; Yoon, W.-S. Advances in the Cathode Materials for Lithium Rechargeable Batteries. *Angew. Chem., Int. Ed.* **2020**, *59*, 2578−2605.
(22) Li, S.; Yao, Z.; Zheng, J.; Fu, M.; Cen, J.; Hwang, S.; Jin, H.; Orlov, A.; Gu, L.; Wang, S.; Chen, Z.; Su, D. Direct Observation of Defect-Aided Structural Evolution in a Nickel-Rich Layered Cathode. *Angew. Chem., Int. Ed.* **2020**, *59*, 22092−22099.
(23) Yoon, M.; Dong, Y.; Hwang, J.; Sung, J.; Cha, H.; Ahn, K.; Huang, Y.; Kang, S. J.; Li, J.; Cho, J. Reactive boride infusion stabilizes Ni-rich cathodes for lithium-ion batteries. *Nat. Energy* **2021**, *6*, 362−371.
(24) Liu, Y.; Lin, X. J.; Sun, Y. G.; Xu, Y. S.; Chang, B. B.; Liu, C. T.; Cao, A. M.; Wan, L. J. Precise Surface Engineering of Cathode Materials for Improved Stability of Lithium-Ion Batteries. *Small* **2019**, *15*, No. e1901019.
(25) Seong, W. M.; Cho, K.-H.; Park, J.-W.; Park, H.; Eum, D.; Lee, M. H.; Kim, I.-s. S.; Lim, J.; Kang, K. Controlling Residual Lithium in High-Nickel (>90 %) Lithium Layered Oxides for Cathodes in Lithium-Ion Batteries. *Angew. Chem., Int. Ed.* **2020**, *59*, 18662−18669.
(26) Zhang, F.; Lou, S.; Li, S.; Yu, Z.; Liu, Q.; Dai, A.; Cao, C.; Toney, M. F.; Ge, M.; Xiao, X.; Lee, W. K.; Yao, Y.; Deng, J.; Liu, T.; Tang, Y.; Yin, G.; Lu, J.; Su, D.; Wang, J. Surface regulation enables high stability of single-crystal lithium-ion cathodes at high voltage. *Nat. Commun.* **2020**, *11*, 3050.
(27) Yang, L.; Chen, R.; Liu, Z.; Gao, Y.; Wang, X.; Wang, Z.; Chen, L. Configuration-dependent anionic redox in cathode materials. *Battery Energy* **2022**, *1*, 20210015.
(28) Zou, L.; He, Y.; Liu, Z.; Jia, H.; Zhu, J.; Zheng, J.; Wang, G.; Li, X.; Xiao, J.; Liu, J.; Zhang, J.-G.; Chen, G.; Wang, C. Unlocking the passivation nature of the cathode−air interfacial reactions in lithium ion batteries. *Nat. Commun.* **2020**, *11*, 3204.
(29) Lu, S.-Q.; Guo, S.-J.; Qi, M.-Y.; Li, J.-Y.; Cao, A.-M.; Wan, L.-J. Precise surface control of cathode materials for stable lithium-ion batteries. *Chem. Commun.* **2022**, *58*, 1454−1467.
(30) Xin, F.; Zhou, H.; Zong, Y.; Zuba, M.; Chen, Y.; Chernova, N. A.; Bai, J.; Pei, B.; Goel, A.; Rana, J.; Wang, F.; An, K.; Piper, L. F. J.; Zhou, G.; Whittingham, M. S. What is the Role of Nb in Nickel-Rich Layered Oxide Cathodes for Lithium-Ion Batteries? *ACS Energy Lett.* **2021**, *6*, 1377−1382.
(31) Yan, P.; Zheng, J.; Liu, J.; Wang, B.; Cheng, X.; Zhang, Y.; Sun, X.; Wang, C.; Zhang, J.-G. Tailoring grain boundary structures and chemistry of Ni-rich layered cathodes for enhanced cycle stability of lithium-ion batteries. *Nat. Energy* **2018**, *3*, 600−605.
(32) Xu, G.-L.; Liu, Q.; Lau, K. K. S.; Liu, Y.; Liu, X.; Gao, H.; Zhou, X.; Zhuang, M.; Ren, Y.; Li, J.; Shao, M.; Ouyang, M.; Pan, F.; Chen, Z.; Amine, K.; Chen, G. Building ultraconformal protective layers on both secondary and primary particles of layered lithium transition metal oxide cathodes. *Nat. Energy* **2019**, *4*, 484−494.
(33) Chen, Z.; Kim, G.-T.; Bresser, D.; Diemant, T.; Asenbauer, J.; Jeong, S.; Copley, M.; Behm, R. J.; Lin, J.; Shen, Z.; Passerini, S. $MnPO_4$-Coated $Li(Ni_{0.4}Co_{0.2}Mn_{0.4})O_2$ for Lithium(-Ion) Batteries with Outstanding Cycling Stability and Enhanced Lithiation Kinetics. *Adv. Eng. Mater.* **2018**, *8*, 1801573.
(34) Lin, X.-J.; Sun, Y.-G.; Guo, S.-J.; Zhang, S.-D.; Liu, Y.; Cao, A.-M. Kinetically-controlled formation of Fe_2O_3 nanoshells and its potential in Lithium-ion batteries. *Chem. Eng. J.* **2022**, *433*, 133188.
(35) Tripathy, N.; Ahmad, R.; Jeong, H.-S.; Hahn, Y.-B. Time-Dependent Control of Hole-Opening Degree of Porous ZnO Hollow Microspheres. *Inorg. Chem.* **2012**, *51*, 1104−1110.
(36) Lin, R.; Bak, S.-M.; Shin, Y.; Zhang, R.; Wang, C.; Kisslinger, K.; Ge, M.; Huang, X.; Shadike, Z.; Pattammattel, A.; Yan, H.; Chu, Y.; Wu, J.; Yang, W.; Whittingham, M. S.; Xin, H. L.; Yang, X.-Q. Hierarchical nickel valence gradient stabilizes high-nickel content layered cathode materials. *Nat. Commun.* **2021**, *12*, 2350.
(37) Wu, Z. Z.; Ji, S. P.; Hu, Z. X.; Zheng, J. X.; Xiao, S.; Lin, Y.; Xu, K.; Amine, K.; Pan, F. Pre-lithiation of $Li(Ni_{1-x-y}Mn_xCo_y)O_2$ Materials Enabling to Enhance Performance for Li-Ion Battery. *ACS Appl. Mater. Interfaces* **2016**, *8*, 15361−15368.
(38) Moeez, I.; Susanto, D.; Ali, G.; Jung, H. G.; Lim, H. D.; Chung, K. Y. Effect of the Interfacial Protective Layer on $NaFe_{0.5}Ni_{0.5}O_2$ Cathode for Rechargeable Sodium-Ion Batteries. *J. Mater. Chem. A* **2020**, *8*, 13964−13970.
(39) Liu, X.; Xu, G. L.; Yin, L.; Hwang, I.; Li, Y.; Lu, L.; Xu, W.; Zhang, X.; Chen, Y.; Ren, Y.; Sun, C. J.; Chen, Z.; Ouyang, M.;

https://doi.org/10.1021/jacs.2c13787
J. Am. Chem. Soc. 2023, 145, 7397−7407

Amine, K. Probing the Thermal-Driven Structural and Chemical Degradation of Ni-Rich Layered Cathodes by Co/Mn Exchange. *J. Am. Chem. Soc.* **2020**, *142*, 19745−19753.
(40) Zou, Y. G.; Meng, F. Q.; Xiao, D. D.; Sheng, H.; Chen, W. P.; Meng, X. H.; Du, Y. H.; Gu, L.; Shi, J. L.; Guo, Y. G. Stable Interfacial Phase on Single-Crystalline Ni-Rich Cathode via Chemical Reaction with Phosphomolybdic Acid. *Nano Energy* **2021**, *87*, 106172.
(41) Yan, P.; Zheng, J.; Lv, D.; Wei, Y.; Zheng, J.; Wang, Z.; Kuppan, S.; Yu, J.; Luo, L.; Edwards, D.; Olszta, M.; Amine, K.; Liu, J.; Xiao, J.; Pan, F.; Chen, G.; Zhang, J.-G.; Wang, C.-M. Atomic-Resolution Visualization of Distinctive Chemical Mixing Behavior of Ni, Co, and Mn with Li in Layered Lithium Transition-Metal Oxide Cathode Materials. *Chem. Mater.* **2015**, *27*, 5393−5401.
(42) Bao, W.; Qian, G.; Zhao, L.; Yu, Y.; Su, L.; Cai, X.; Zhao, H.; Zuo, Y.; Zhang, Y.; Li, H.; Peng, Z.; Li, L.; Xie, J. Simultaneous Enhancement of Interfacial Stability and Kinetics of Single-Crystal $LiNi_{0.6}Mn_{0.2}Co_{0.2}O_2$ through Optimized Surface Coating and Doping. *Nano Lett.* **2020**, *20*, 8832−8840.
(43) Fan, X.; Ou, X.; Zhao, W.; Liu, Y.; Zhang, B.; Zhang, J.; Zou, L.; Seidl, L.; Li, Y.; Hu, G.; Battaglia, C.; Yang, Y. In situ inorganic conductive network formation in high-voltage single-crystal Ni-rich cathodes. *Nat. Commun.* **2021**, *12*, 5320.
(44) Zhang, W.; Sun, X. L.; Tang, Y. X.; Xia, H. R.; Zeng, Y.; Qiao, L.; Zhu, Z. Q.; Lv, Z. S.; Zhang, Y. Y.; Ge, X.; Xi, S. B.; Wang, Z. G.; Du, Y. H.; Chen, X. D. Lowering Charge Transfer Barrier of $LiMn_2O_4$ via Nickel Surface Doping to Enhance Li+ Intercalation Kinetics at Subzero-Temperatures. *J. Am. Chem. Soc.* **2019**, *141*, 14038−14042.
(45) Xia, H. R.; Zhang, W.; Cao, S. K.; Chen, X. D. A Figure of Merit for Fast-Charging Li-ion Battery Materials. *ACS Nano* **2022**, *16*, 8525−8530.
(46) Liu, Y.; Tang, L. B.; Wei, H. X.; Zhang, X. H.; He, Z. J.; Li, Y. J.; Zheng, J. C. Enhancement on structural stability of Ni-rich cathode materials by in-situ fabricating dual-modified layer for lithium-ion batteries. *Nano Energy* **2019**, *65*, 104043.
(47) Giordano, L.; Østergaard, T. M.; Muy, S.; Yu, Y.; Charles, N.; Kim, S.; Zhang, Y.; Maglia, F.; Jung, R.; Lund, I.; Rossmeisl, J.; Shao-Horn, Y. Ligand-Dependent Energetics for Dehydrogenation: Implications in Li-Ion Battery Electrolyte Stability and Selective Oxidation Catalysis of Hydrogen-Containing Molecules. *Chem. Mater.* **2019**, *31*, 5464−5474.
(48) Zou, L.; Li, J.; Liu, Z.; Wang, G.; Manthiram, A.; Wang, C. Lattice doping regulated interfacial reactions in cathode for enhanced cycling stability. *Nat. Commun.* **2019**, *10*, 3447.

https://doi.org/10.1021/jacs.2c13787
J. Am. Chem. Soc. 2023, 145, 7397−7407